CCAV-10m: An Annual Spatiotemporal China's Coastal Wetland Vegetation Dataset Integrating Sentinel-1/2 Observations via Deep Learning

Yuying Li[1,2], Lina Yuan[1,2], Ting Liu[1,2], Zijiang Song[1,2], Shuang Yang[1,2], Zilong Zhu[1,2], and Min Liu[1,2]

[1]Key Laboratory of Geographic Information Science (Ministry of Education), East China Normal University, Shanghai 200241, China
[2]Key Laboratory of Spatial-temporal Big Data Analysis and Application of Natural Resources in Megacities (Ministry of Natural Resources), East China Normal University, Shanghai 200241, China

Correspondence: Lina Yuan (lnyuan@geoai.ecnu.edu.cn) and Min Liu (mliu@geo.ecnu.edu.cn)

Abstract. Coastal wetland vegetation plays a vital role in shoreline protection and ecosystem management, highlighting the need for accurate and high-resolution mapping of these unique and vulnerable habitats. Here, we present CCAV-10m, the first publicly available annual species-level coastal wetland dataset for China at 10 m resolution (2016–2023). This dataset was generated using a novel phenology-guided coastal wetland vegetation classification network (P_SVCN), which integrates Sentinel-1/2 satellite imagery with extensive in situ observations. Validation based on 4,668 in situ samples confirms that P_SVCN delivers strong classification performance, achieving an overall accuracy of 0.916 and a Kappa coefficient of 0.898. Spatiotemporal analysis of CCAV-10m reveals that *Suaeda spp.* is the dominant vegetation type, followed by *S. alterniflora*, whose coverage nearly equals the combined extent of *P. australis*, mangroves, *S. mariqueter*, and *T. chinensis*. Notably, this work fills critical gaps in both spatial detail and temporal consistency across existing coastal wetland datasets, demonstrating the effectiveness of deep-learning-based fusion of optical and SAR data for high-resolution vegetation mapping. Regular updates to CCAV-10m will support long-term coastal wetland research, enhance invasive species monitoring, and inform wetland restoration and precision management efforts. The CCAV-10m dataset is openly accessible at https://doi.org/10.57760/sciencedb.31077 (Li et al., 2025).

1 Introduction

Coastal wetlands are complex ecosystems distributed along the land–sea transition zone, influenced jointly by tidal dynamics and salinity gradients, and mainly comprise salt marshes, mangroves, tidal flats, and brackish wetland forests (Day et al., 2024; Bernhardt, 2022; Moreno-Mateos et al., 2012). Tropical mangroves cover approximately 150,000 km^2, while temperate tidal marshes exceed 45,000 km^2 (Webb et al., 2013; Luther and Greenberg, 2009), together forming one of the most productive and carbon-rich ecosystems on earth (Macreadie et al., 2019; Bertram et al., 2021). Coastal wetlands function not only as geochemical "sinks" but also as highly effective "green filters" that intercept and remove land-derived pollutants (Sun et al., 2015; Zhang et al., 2022c). Their ecosystem service value can reach up to US$194,000 per hectare per year, encompassing carbon sequestration and greenhouse gas regulation, coastal protection, fisheries support, water purification, and biodiversity

maintenance (Gabler et al., 2017; Schuerch et al., 2018; Costanza et al., 2014; Duarte et al., 2013; Aburto-Oropeza et al., 2008).
China's coastal wetlands represent a key component of its national blue carbon ecosystems, spanning tropical, subtropical, and
25 temperate climate zones (Cao and Wong, 2007; Sun et al., 2015; Wang et al., 2021). Their broad distribution and substantial
carbon sequestration capacity place them at the core of China's blue carbon strategy (Gu et al., 2025). Dominant vegetation
types in Chinese coastal wetlands include *S. alterniflora*, *P. australis*, *T. chinensis*, *Suaeda spp.*, *S. mariqueter*, and mangroves
(Gu et al., 2021). Among these, *S. alterniflora*, introduced in the 1990s, has rapidly expanded across Jiangsu, Shanghai, Zhe-
jiang, and Fujian, with scattered occurrences in Liaoning, Tianjin, Hebei, and Shandong (Min et al., 2025; Chen et al., 2025).
30 In many East Asian countries, biological invasions, tidal flat reclamation, and wetland restoration occur simultaneously; thus,
timely and fine-scale species-level monitoring is crucial for tracking invasion dynamics, evaluating restoration outcomes, and
supporting biodiversity conservation and sustainable coastal management (Tian et al., 2020; Sun et al., 2023).

Coastal wetlands are composed of herbaceous plants, grasses, and low-stature shrubs that are adapted to regular or occasional
tidal inundation (Kumar and Sinha, 2014). Due to the inherent complexity of vegetation, tidal dynamics, and anthropogenic
35 disturbances, mapping of coastal wetlands remains challenging (Zhao et al., 2023). To date, a variety of remote sensing data
sources have been widely applied to monitor coastal wetland vegetation. In multispectral optical imagery, medium- to low-
resolution datasets such as MODIS and AVHRR offer high temporal resolution (Gallo et al., 2005; Zhang et al., 2023a), which
makes them suitable for wetland information extraction; however, their spatial resolution is insufficient for vegetation species-
level classification (Takeuchi et al., 2003; Zhang et al., 2019). High-resolution optical imagery also plays an important role in
40 wetland vegetation classification, but it is limited by cloud cover and atmospheric effects (Kang et al., 2023; O'Connell et al.,
2017). Moreover, traditional remote sensing methods based on vegetation indices and phenological features are still widely
applied. For example, the enhanced phenology-based vegetation index algorithm proposed by Zeng et al. (2022) achieved an
overall accuracy of 86.67% for coastal salt marshes along the Bohai Sea, while Sun et al. (2023) applied a time-series model
and phenological parameters to classify Jiangsu coastal salt marshes with an average overall accuracy of 84.8% (±5.5%).
45 Although these approaches are effective for short-term monitoring, they often struggle to capture complex spatial structures
and inter-annual dynamics fully.

With the advancement of remote sensing technology, research on wetland vegetation classification has gradually shifted from
traditional optical image-based methods to multi-source data fusion techniques. Synthetic Aperture Radar (SAR), with its all-
weather and all-time imaging capabilities, has become a key complement to optical imagery (Van Beijma et al., 2014; Veloso
50 et al., 2017). In recent years, researchers have attempted to integrate SAR and optical imagery to improve the accuracy of salt
marsh vegetation classification. For instance, Xu et al. (2025) integrated Sentinel-1 SAR and Sentinel-2 optical imagery to
classify wetland vegetation in the Yellow River Delta, China, achieving an overall accuracy of 93.51% and a Kappa coefficient
of 0.917. Similarly, Slagter et al. (2020) combined Sentinel-1 SAR and Sentinel-2 for multi-level wetland classification in the
St. Lucia Wetlands, South Africa, with an overall accuracy of 90.7%. At the same time, with the development of deep learning,
55 convolutional neural networks and attention mechanisms have been increasingly applied to wetland vegetation classification,
significantly improving spatial detail representation and cross-temporal feature extraction. For example, Sun et al. (2025)
employed a hybrid 2D–3D CNN to achieve an annual average classification accuracy exceeding 97% for Jiangsu coastal

wetlands, and Li et al. (2021a) used a U-Net model to classify wetlands in South Carolina, USA, achieving a maximum
accuracy of 90%. Although these regional studies have achieved promising results, they mostly focus on single-date or short-
60 term analyses. Therefore, long-term, species-level wetland monitoring at a national scale remains limited, which is crucial for
coastal ecosystem management and wetland conservation.

In this study, we developed a novel phenology-guided coastal wetland vegetation classification network integrating Sentinel-
1/2 (P_SVCN) based on deep learning and employed it to generate the CCAV-10m dataset (https://doi.org/10.57760/sciencedb.
31077, Li et al., 2025), an annual spatiotemporal China's coastal wetland vegetation dataset, 2016–2023. The P_SVCN model
65 integrates Sentinel-1 and Sentinel-2 imagery with in situ data, maintaining the sensitivity of SAR data to vegetation structure
and moisture while adaptively incorporating the spectral and phenological information from optical imagery. P_SVCN signif-
icantly improves classification accuracy, enabling species-level mapping of coastal wetland vegetation. CCAV-10m provides
a valuable spatiotemporal resource for long-term monitoring, ecological research, and sustainable management of China's
coastal wetlands.

70 **2   Study area**

The Chinese coastline extends approximately 32,000 km, including 14,000 km of island coastlines, ranging from the Yalu
River estuary in northern Liaoning Province to the Beilun River estuary in southern Guangxi and Hainan Island (Gu et al.,
2021, 2025). This study focuses on eight coastal provinces and municipalities: Liaoning, Hebei, Tianjin, Shandong, Jiangsu,
Shanghai, Zhejiang, and Fujian, spanning 23°30′– 40°03′ N latitude and 115°50′– 124°22′ E longitude (Fig. 1). The study
75 area covers both temperate and subtropical climatic zones, supporting a diverse range of wetland vegetation types (Hu et al.,
2021). Wetland boundaries were delineated using the GLC_FCS30D dataset (Zhang et al., 2023b), with a 10 km buffer inland
and seaward from the coastline applied for analysis. Common wetland species include *S. alterniflora*, *P. australis*, *T. chinensis*,
Suaeda spp., *S. mariqueter*, and mangroves (Chen et al., 2022). *S. alterniflora*, native to the Americas, was introduced to China
in the 1990s and is now widespread in Jiangsu, Shanghai, Zhejiang, and Fujian, with scattered occurrences in Liaoning, Tianjin,
80 Hebei, and Shandong (Min et al., 2025; Chen et al., 2025). *S. mariqueter* occurs mainly in Shanghai, Jiangsu, and the Hangzhou
Bay area (Sun et al., 2025; Zheng et al., 2023), while *T. chinensis* and *Suaeda spp.* are concentrated in northern provinces (Sun
et al., 2021), and mangroves are restricted to the southern coast, reaching their northern limit in Yueqing, Zhejiang (Wei et al.,
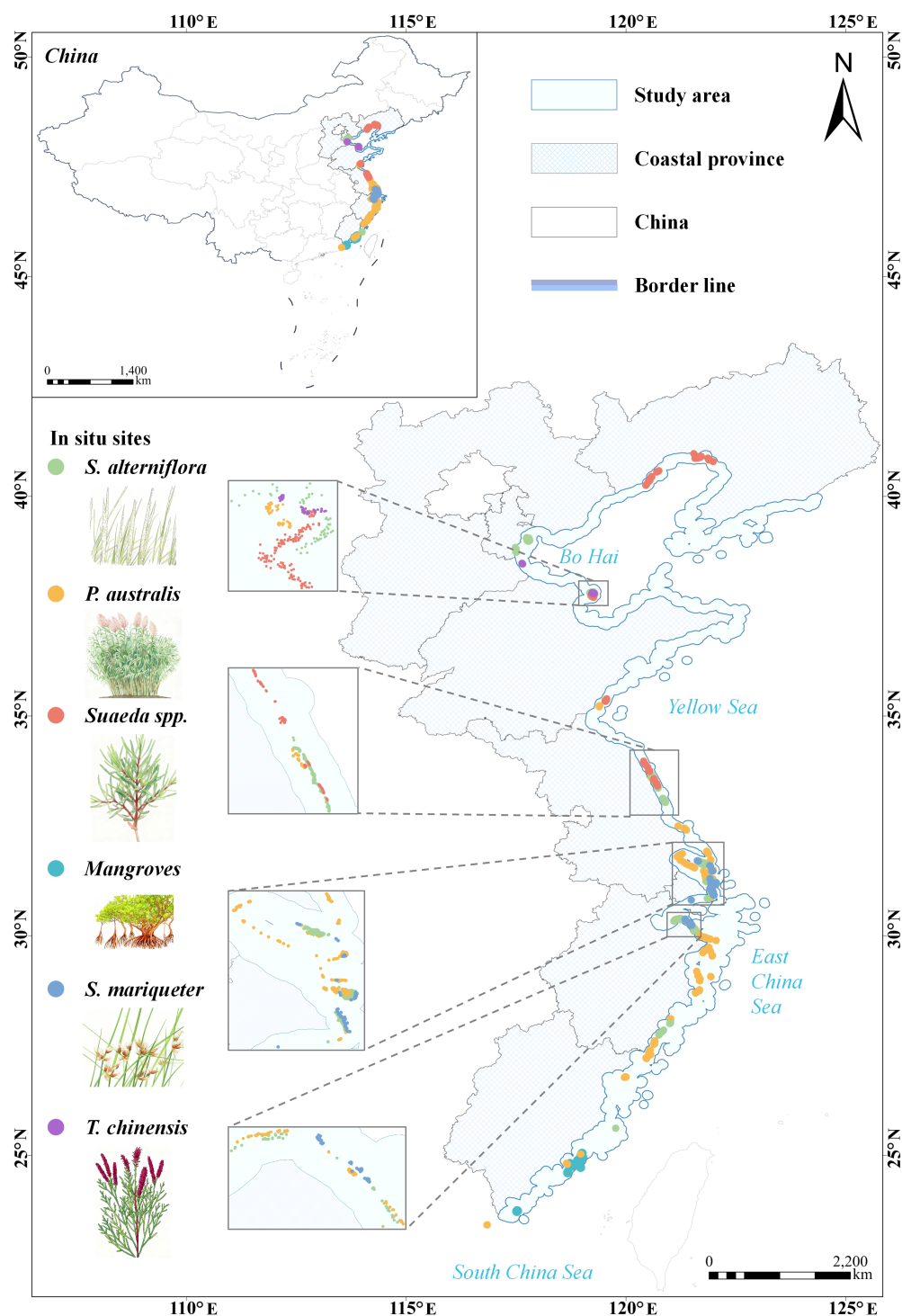2024).

Figure 1. Location of the study area along the Chinese coastline, showing the extent of the coastal zone and the distribution of in situ wetland sampling sites.

Earth System
Science
Data

3 Data and methods

3.1 Sentinel-1

We used multisource remote sensing data, including Sentinel-1 and Sentinel-2 imagery, to improve coastal vegetation classification (Zhao et al., 2024). Sentinel-1 Level-1 Ground Range Detected (GRD) data (Potin et al., 2015) at 10 m resolution were preprocessed in SNAP following orbital correction, thermal noise removal, radiometric calibration, speckle filtering, and terrain correction, with reflectivity converted from linear scale to decibels (dB) (Li et al., 2024b). A total of 8,018 scenes spanning January 2016 to December 2023 in China were composited annually using a mean function. These composites captured regional climatic patterns while reducing tidal and seasonal variability in salt marsh vegetation.

3.2 Sentinel-2

Sentinel-2 imagery was selected according to key phenological stages of coastal vegetation, namely green and senescence (Zhao et al., 2023). Across the study period, 320 scenes were processed in SNAP and ENVI, including resampling and band fusion (Wang et al., 2024). For each phenophase, four spectral bands with the highest vegetation contrast—B02 (blue), B03 (green), B04 (red), and B08 (near-infrared)—were extracted, yielding eight optical channels (Bao et al., 2025). Normalized Difference Vegetation Index (NDVI) maps were derived from red and near-infrared bands of both phenophases to capture differences in vegetation status. All SAR and optical images were co-registered and resampled to a consistent 10 m resolution to ensure data alignment and comparability.

3.3 In situ data

We conducted field surveys and vegetation sampling across wetlands along the coast of China, between 2017 and 2018. High-precision GPS (Trimble Juno 3D) and a DJI Phantom-4 RTK unmanned aerial vehicle were combined to systematically record site information. Following a stratified sampling design, plots were established for six representative salt marsh vegetation types: *P. australis*, *S. alterniflora*, *Suaeda spp.*, *T. chinensis*, mangroves, and *S. mariqueter*. Each plot measured 10 × 10 m, with a minimum distance of 100 m between adjacent plots to ensure spatial independence and representativeness. Within each plot, three 0.5 × 0.5 m quadrats were randomly located. GPS coordinates of each quadrat were recorded with ±5 m accuracy to guarantee even spatial coverage across vegetation types. Plot locations were further verified and corrected using high-resolution imagery from Google Earth to ensure consistency with actual vegetation distribution. To complement the field data, we also compiled additional wetland vegetation validation points from the literature (Zhao et al., 2023; Li et al., 2021b; Sun, 2023).

In total, 2,665 ground truth points were collected (Fig. 1), comprising 948 *S. alterniflora*, 678 *P. australis*, 432 *Suaeda spp.*, 226 *S. mariqueter*, 263 mangrove, and 118 *T. chinensis* points. Experienced researchers then conducted visual interpretation and manual labeling of additional points using Google Earth imagery, resulting in 2,072 *S. alterniflora*, 2,435 *P. australis*, 2,632 *Suaeda spp.*, 2,901 *S. mariqueter*, 1,803 mangrove, and 1,050 *T. chinensis* points. Collected samples underwent systematic quality control, producing a reliable dataset for training and validating remote sensing classification models.

3.4 A phenology-guided coastal wetland vegetation classification network integrating Sentinel-1/2 (P_SVCN)

In this study, we developed a phenology-guided coastal wetland vegetation classification network integrating Sentinel-1/2 (P_SVCN) with a dual-branch multi-source attention mechanism for the fine-scale classification of coastal wetland vegetation along the Chinese coast. The training dataset was based on Sentinel-1 imagery from 2017–2018, including VV and VH polarizations, along with three derived SAR features (SAR-Diff, SAR-NDVI, and SAR-SUM). Simultaneously, dual-phase Sentinel-2 optical imagery was incorporated, extracting eight spectral bands (B02, B03, B04, and B08 at two phenological phases) and their corresponding NDVI indices as input features. Vegetation types recorded at the sampled locations corresponding to the imagery periods were used as ground truth for supervised training. The dataset was strictly split into training (70%, 10,890 samples) and validation (30%, 4,668 samples) subsets. The trained model was then applied to classify coastal wetland vegetation from 2016 to 2023 along the Chinese coast.

3.4.1 SAR feature construction from Sentinel-1

Sentinel-1 SAR imagery offers significant advantages for monitoring wetland vegetation, being highly sensitive to key variables such as total vegetation water content, canopy structure dynamics, and vegetation cover (Vreugdenhil et al., 2018; Zhang et al., 2022a). With its all-weather, all-time radar observation capability, Sentinel-1 can reliably acquire data under diverse meteorological conditions, providing robust support for temporal analyses of vegetation dynamics (Simioni et al., 2020; Mleczko and Mróz, 2018). The C-band radar signals can penetrate the canopy and effectively capture interactions between vegetation and soil (Mao et al., 2023), making Sentinel-1 particularly suitable for long-term monitoring and dynamic studies of wetland ecosystems (Yang and Guo, 2019; Zhang et al., 2021).

Backscatter coefficients in VV and VH polarization provide insight into vegetation–ground interactions (Vreugdenhil et al., 2018; Mandal et al., 2020; Nikaein et al., 2021). Vegetated areas typically exhibit higher surface roughness than non-vegetated regions, resulting in distinct backscatter differences, although VH polarization signals may be influenced by double-bounce effects from soil surfaces (Veloso et al., 2017; Ferro et al., 2011). Based on these considerations, this study utilized VV and VH single-polarization SAR data along with three derived indices—SAR_NDVI, SAR_SUM, and SAR_Diff—for the classification of wetland vegetation types along China's coastal.

SAR_NDVI quantifies normalized differences in backscatter coefficients between VV and VH polarization states, providing a reliable basis for distinguishing vegetation types (Veloso et al., 2017). SAR_Diff effectively suppresses double-bounce effects from straw or surface structures, enhancing the ability to detect subtle differences between vegetation and soil, thereby improving classification accuracy (Mahdianpari et al., 2020). SAR_SUM integrates the total backscatter intensity from both VV and VH channels, offering a comprehensive representation of canopy and surface structure information (Li et al., 2024b).

3.4.2 Phenology-based spectral feature extraction from Sentinel-2

The dominant vegetation types in different climatic zones exhibit distinct phenological rhythms (Zhang et al., 2022b). In temperate regions, vegetation growth is constrained by low temperatures and dormancy periods, resulting in a relatively con-

centrated growing season (Luo et al., 2025), whereas in subtropical regions, the growing period is prolonged and phenological transitions are relatively gradual. Using imagery acquired at a uniform time across the entire coastal zone would lead to phenological mismatches among regions, thereby increasing spectral confusion and classification errors (Zeng et al., 2022).
Therefore, this study adopted a climate-zone–based strategy, selecting paired images corresponding to the green and senescence stages within each zone to enhance the spectral separability among vegetation types. To fully leverage the spectral differences of coastal wetland vegetation across phenological stages (Gao et al., 2023; Fu et al., 2025), dual-phase optical imagery was selected based on the growth patterns of representative vegetation within each climatic zone.

The annual NDVI time series of dominant coastal vegetation types along the coast of China (Fig. 2) clearly reveal distinct seasonal dynamics for each species. The temperate zone was defined as the area north of the Qinling–Huaihe line (approximately 33°N), where the mean January temperature is below 0 °C (Almond et al., 2009; Chen et al., 2013), primarily including the coastal provinces of Liaoning, Tianjin, Hebei, Shandong, and northern Jiangsu. The North Subtropical zone extends from the Qinling–Huaihe line southward to the northernmost mangrove distribution in Yueqing, Zhejiang ($\approx$28°21′N) (You et al., 2022), covering southern Jiangsu, Shanghai, and northern Zhejiang. The Subtropical zone lies south of this boundary, encompassing southern Zhejiang and Fujian provinces. For the temperate, North Subtropical, and Subtropical regions, two key time points (t_1 and t_2) corresponding to the peak growth and senescence stages were identified. Within each climatic zone, the dual-phase selection was kept consistent to ensure uniform input features. For spectral feature construction, four key optical bands—blue (B2), green (B3), red (B4), and near-infrared (B8)—were extracted for each pixel at both phenological stages, and the Normalized Difference Vegetation Index (NDVI) was calculated from the red and near-infrared bands(Eq. 1). The dual-phase optical bands and corresponding NDVI values were then combined into a spectral feature vector(Eq. 2).

$$\text{NDVI} = \frac{\text{NIR} - \text{Red}}{\text{NIR} + \text{Red}} \tag{1}$$

$$\mathbf{F}_{\text{spectral}} = [B2_{t1}, B3_{t1}, B4_{t1}, B8_{t1}, NDVI_{t1}, B2_{t2}, B3_{t2}, B4_{t2}, B8_{t2}, NDVI_{t2}] \tag{2}$$
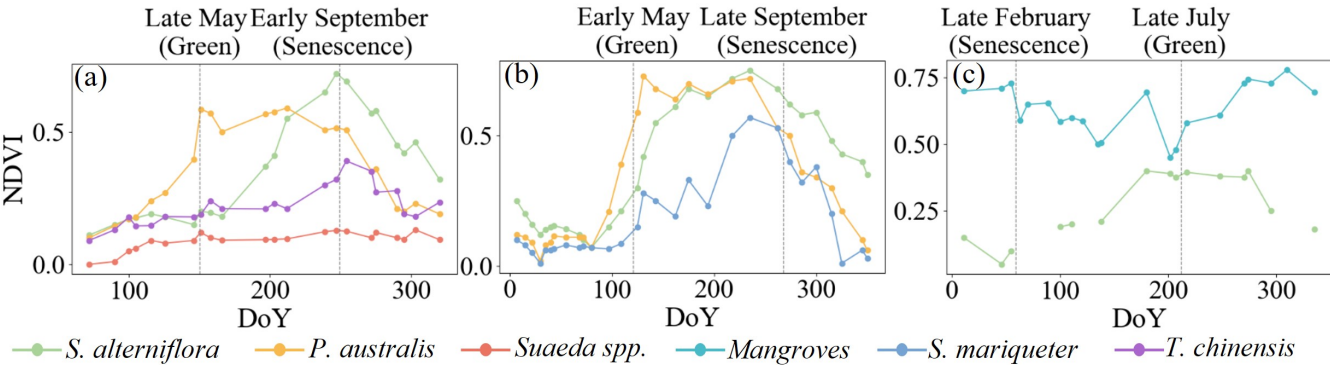
Figure 2. Seasonal NDVI of dominant coastal wetland vegetation along the coast of China. (a) Temperate, (b) North Subtropical, and (c) Subtropical zones. Distinct annual NDVI variations were observed among the main vegetation types (*S. alterniflora*, *P. australis*, *Suaeda spp.*, *S. mariqueter*, *T. chinensis*, and mangroves), which guided the dual-phase selection summarized in Tab 1.

Table 1. Dual-phase phenological information of wetland vegetation across different climatic zones along the coast of China. This table summarizes the representative vegetation types, selected phenological phases, and the rationale for determining optimal dual-phase optical imagery in temperate, north subtropical, and subtropical regions.

Climatic Zone	Vegetation Types	Phase 1 (Green)	Phase 2 (Senescence)	Selection Rationale
Temperate (Liaoning, Tianjin, Hebei, Shandong, Jiangsu)	*S. alterniflora*, *P. australis*, *Suaeda spp.*, *T. chinensis*	Late May	Early September	Late May: *P. australis* greening advanced while *S. alterniflora* has not peaked; Early September: *S. alterniflora* near peak and *P. australis* declining. Maximizes phenological contrast between *P. australis* and *S. alterniflora*, and distinguishes *T. chinensis* (low NDVI) from consistently low NDVI *Suaeda spp.*.
North Subtropical (Jiangsu, Shanghai, north of Yueqing, Zhejiang)	*S. alterniflora*, *P. australis*, *S. mariqueter*, *Suaeda spp.*	Early May	Late September	Early May: growth differences among *S. mariqueter*, *P. australis*, and *S. alterniflora* are pronounced; Late September: senescence differentiates *P. australis* and *S. alterniflora*
Subtropical (Zhejiang, Fujian)	*S. alterniflora*, mangroves	Late July	Late February	Late July: *S. alterniflora* at peak, distinguishable from evergreen mangroves; Late February: *S. alterniflora* NDVI lowest, clearly distinguishable from mangroves.

Earth System
Science
Data

3.4.3 Network framework of the P_SVCN

Coastal wetland vegetation often exhibits high spectral similarity, further complicated by tidal fluctuations, salinity gradients,
170   and seasonal phenology, which challenge accurate classification (Gao et al., 2023; Fu et al., 2025). To address this, we devel-
oped a phenology-guided coastal wetland vegetation classification network integrating Sentinel-1/ (P_SVCN), which employs
a dual-branch multi-source attention fusion design to enhance feature representation (Fig. 3). One branch processes Sentinel-1
SAR bands and their derived indices, while the other handles Sentinel-2 optical bands and phenological features. Features from
both branches interact through the SAR–Optical Cross-Source (SOCS) Block. Let the output features of the SAR branch be
175   F_{SAR} and those of the optical branch be F_{Optical}, projected into query (Q), key (K), and value (V) spaces as in Eq. (3):

$$Q = W_Q F_{\text{SAR}}, \quad K = W_K F_{\text{Optical}}, \quad V = W_V F_{\text{Optical}} \tag{3}$$

where W_Q, W_K, W_V are learnable parameters. Scaled dot-product attention is then used to compute inter-source correlation
weights (Eq. (4)):

$$A = \text{Softmax}\left(\frac{QK^\top}{\sqrt{d}}\right) \tag{4}$$

180   These weights are applied to reweight the optical features, producing fused multi-source features (Eq. (5)):

$$F_{\text{cross}} = F_{\text{SAR}} + A \cdot V \tag{5}$$

This mechanism retains the sensitivity of SAR to vegetation structure and water content, while adaptively incorporating
optical spectral and phenological information, thereby enhancing feature discriminability. By applying the attention fusion at
multiple hierarchical levels, P_SVCN dynamically adjusts the contribution of each source, effectively distinguishing vegetation
185   types with similar spectral properties but differing temporal and salinity–hydrology conditions.

To fully exploit the advantages of multiple attention mechanisms, the SAR–Optical Cross-Source (SOCS) block employs
three parallel attention operations along the channel dimension: window attention (WA), shifted window attention (SWA),
and long-range attention (LRA) (Song and Zhong, 2022). For an input feature map $T_i \in \mathbb{R}^{H \times W \times C}$, the channels are evenly
split into $K = 3$ groups, each processed by one of the three attention mechanisms. Let the group feature dimensions be
190   $x^{(1)}, x^{(2)}, x^{(3)}$, satisfying $x^{(1)} + x^{(2)} + x^{(3)} = C$. Each group is input to its respective attention module, and the outputs are
concatenated along the channel dimension, forming the SOCS block output:

$$\text{SOCS}(T_i) = \text{Conv}_{1 \times 1}\Big(\text{CAT}\big(\text{WA}(x^{(1)}), \text{SWA}(x^{(2)}), \text{LRA}(x^{(3)})\big)\Big) \tag{6}$$

where $\text{WA}(\cdot)$, $\text{SWA}(\cdot)$, and $\text{LRA}(\cdot)$ denote window attention, shifted window attention, and long-range attention, respectively,
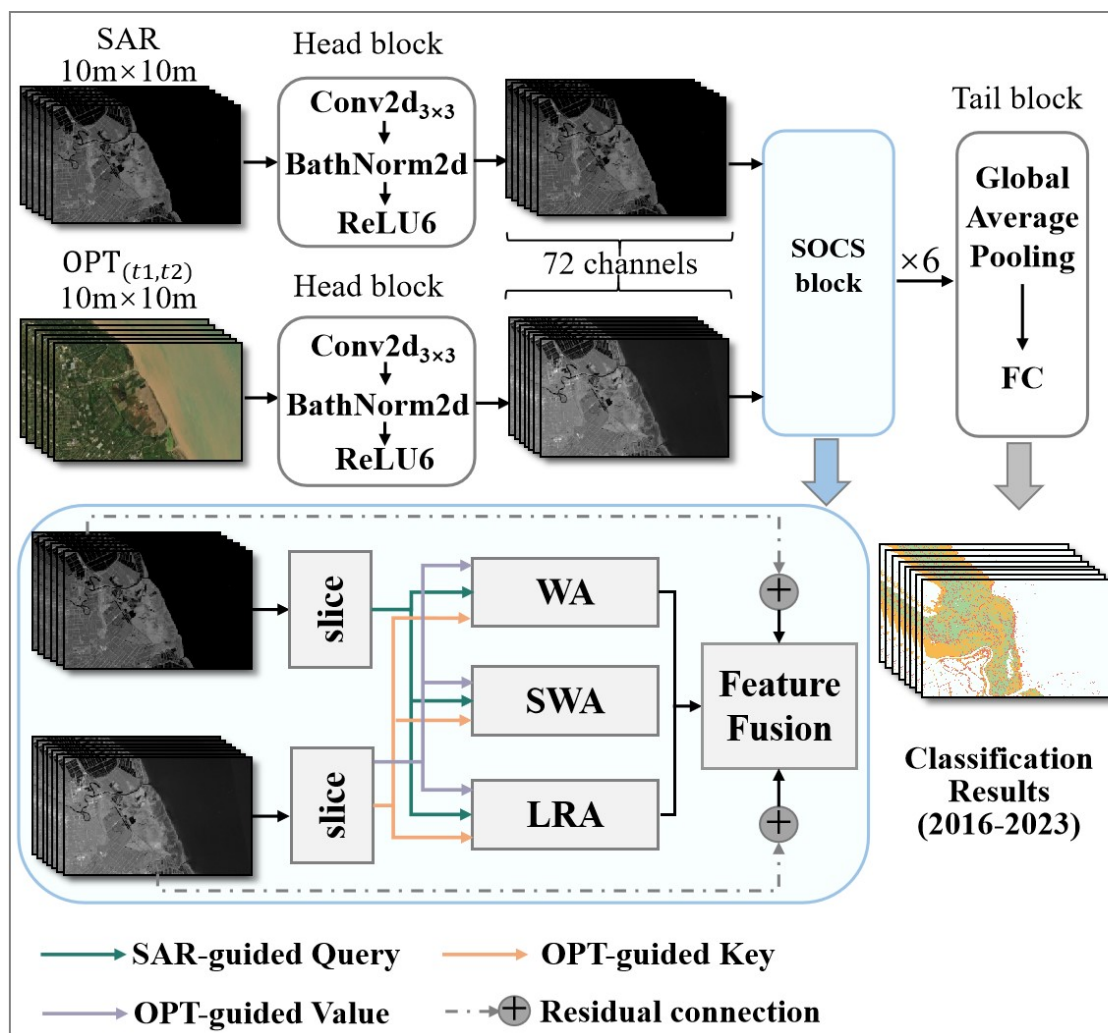195   and $\text{CAT}(\cdot)$ represents channel-wise concatenation.

Figure 3. Architecture of our proposed model, P_SVCN. The network has dual branches for Sentinel-1 SAR and dual-phase Sentinel-2 optical imagery. Each branch begins with a Head Block producing 72-channel features. Features pass through six SOCS blocks with window attention, shifted window attention, and long-range attention, residual connections, and feature fusion. Fused features are pooled globally and fed to a fully connected layer for classification, producing coastal wetland vegetation maps (2016–2023).

3.4.4 Accuracy evaluation of P_SVCN

To evaluate the classification performance of the proposed P_SVCN, an independent accuracy assessment was conducted. All samples were randomly divided into training and validation subsets in a strict 7:3 ratio to ensure a balanced representation of vegetation classes, with 4,668 in situ data points used for model validation.

200　　Model performance was evaluated using a confusion matrix, from which several widely adopted statistical metrics were derived, including Overall Accuracy (OA), Producer's Accuracy (PA), User's Accuracy (UA), F1-score, and the Kappa coefficient (Morales-Barquero et al., 2019). Specifically, the Overall Accuracy (OA), representing the proportion of correctly classified samples among all validation samples, was computed as shown in Eq. (7). The Producer's Accuracy (PA) and User's Accuracy (UA), which quantify omission and commission errors for each class, respectively, were calculated according to Eq. (8). The

205　F1-score, providing a harmonic mean of precision and recall for each class, was computed as in Eq. (9). Finally, the Kappa coefficient, which evaluates the agreement between the classified and reference data beyond random chance, was calculated following Eq. (10).

$$OA = \frac{\sum_{i=1}^{N} n_{ii}}{\sum_{i=1}^{N} \sum_{j=1}^{N} n_{ij}} \tag{7}$$

$$PA_i = \frac{n_{ii}}{\sum_{j=1}^{N} n_{ij}}, \quad UA_i = \frac{n_{ii}}{\sum_{j=1}^{N} n_{ji}} \tag{8}$$

210　$$F1_i = 2 \times \frac{PA_i \times UA_i}{PA_i + UA_i} \tag{9}$$

$$\kappa = \frac{p_o - p_e}{1 - p_e}, \quad p_e = \frac{\sum_{i=1}^{N} \left(\sum_{j=1}^{N} n_{ij} \right) \left(\sum_{j=1}^{N} n_{ji} \right)}{\left(\sum_{i=1}^{N} \sum_{j=1}^{N} n_{ij} \right)^2} \tag{10}$$

　　To further validate the effectiveness of the multi-source attention fusion design, P_SVCN was compared with the Salt marsh Vegetation Classification Network (SVCN) (Li et al., 2024b), a baseline model built upon MobileNet V3. Both models were trained and validated using the same dataset and experimental settings to ensure a fair and reliable comparison. All accuracy

215　metrics were computed in a Python environment using the scikit-learn library. This validation framework provides a systematic and objective basis for quantitatively assessing the advantages of the P_SVCN over single-source approaches in salt marsh vegetation classification.

Earth System
Science
Data

4   Results

4.1   CCAV-10m dataset

220   We present the annual spatiotemporal China's coastal wetland vegetation dataset at 10 m resolution (CCAV-10m), which accurately captures the spatiotemporal dynamics of coastal wetland vegetation types along the coast of China from 2016 to 2023. The dataset has a spatial resolution of 10 m and represents the first publicly released annual time series of coastal wetland vegetation in China. CCAV-10m distinguishes six representative coastal wetland vegetation types—*S. alterniflora*, *P. australis*, *Suaeda spp.*, *S. mariqueter*, mangroves, and *T. chinensis*—achieving species-level classification. Model validation shows a

225   high overall accuracy (OA) of 0.916 and a Kappa coefficient of 0.898, indicating stable and reliable identification across all vegetation types.

In 2023, coastal wetlands in China covered a total area of 617,976.38 ha, comprising six dominant vegetation types: *S. alterniflora*, *P. australis*, *Suaeda spp.*, *S. mariqueter*, *T. chinensis*, and mangroves (Fig. 4). From 2016 to 2023, coastal wetland vegetation exhibited pronounced interannual dynamics across China (Tab. 2), with *Suaeda spp.* as the dominant type, followed

230   by *S. alterniflora*, whose coverage is nearly equivalent to the combined extent of *P. australis*, mangroves, *S. mariqueter*, and *T. chinensis*. *S. alterniflora*, as an invasive saltmarsh species, maintained a relatively stable area, fluctuating between 20,202 ha and 25,918 ha, with occasional declines. *Suaeda spp.* showed a notable increasing trend, expanding from 24,436 ha in 2018 to 35,452 ha in 2023. *P. australis* exhibited considerable interannual variability, reaching its maximum of 22,893 ha in 2020, then decreasing to 10,614 ha in 2023. *T. chinensis* and *S. mariqueter* occupied relatively smaller areas, although *T. chinensis*

235   experienced localized expansion in 2020 and 2022. As a key component of coastal protection, mangroves increased from 4,894 ha in 2017 to 7,648 ha in 2023, showing an overall upward trend.
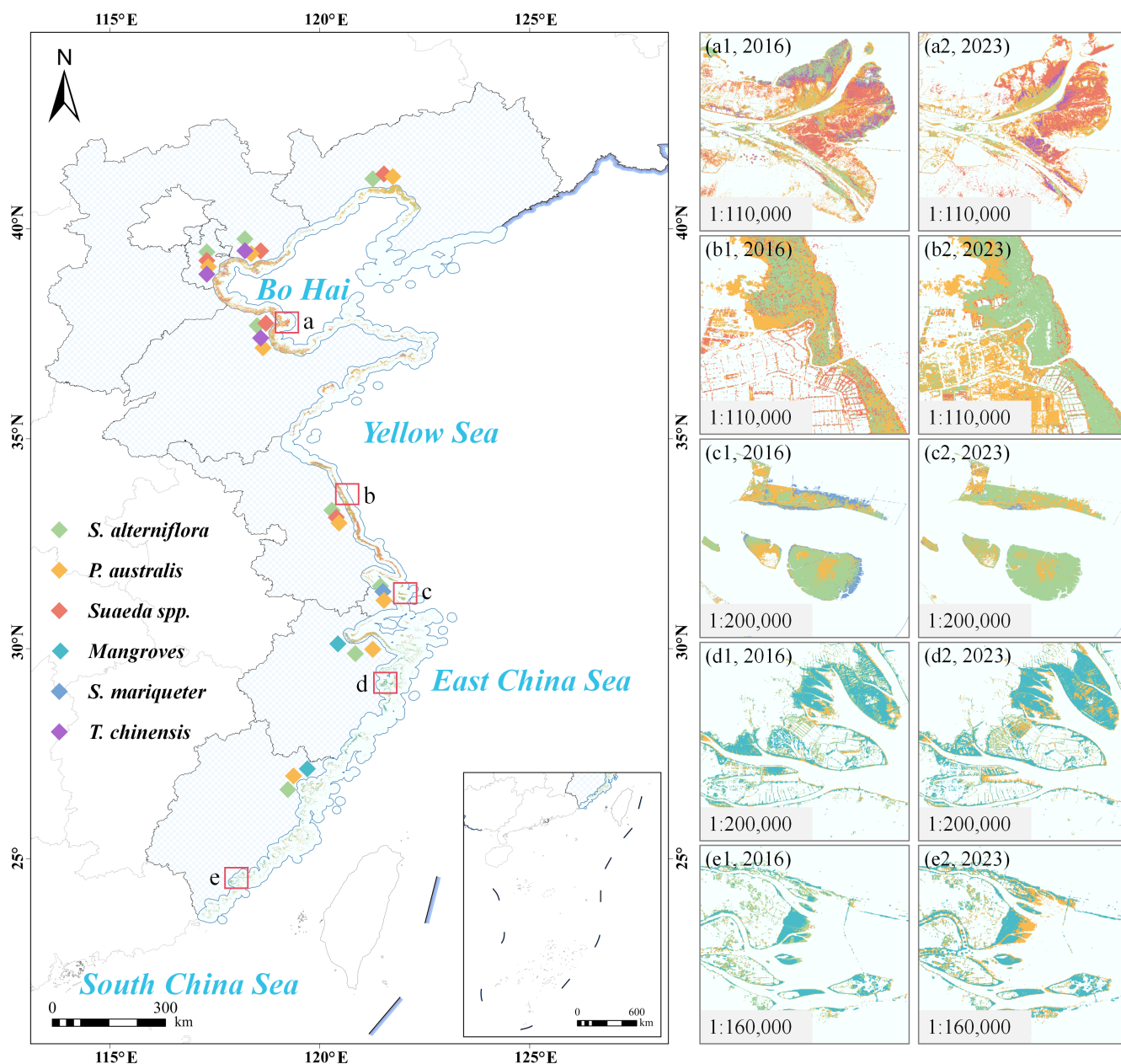
Figure 4. Spatial distribution of coastal wetland vegetation in China and representative regional changes from 2016 to 2023. The main map shows the distribution of dominant coastal wetland species across China in 2023. Insets illustrate the temporal changes in species distribution for key coastal regions: (a1, 2016) and (a2, 2023) represent the Yellow River Estuary; (b1, 2016) and (b2, 2023) represent the Jiangsu coast; (c1, 2016) and (c2, 2023) represent the Yangtze River Estuary; (d1, 2016) and (d2, 2023) represent the Zhejiang coast; and (e1, 2016) and (e2, 2023) represent the Fujian coast.

Table 2. Area of coastal wetland vegetation types in China from 2016 to 2023 (ha). The table summarizes annual changes for six representative vegetation types (*S. alterniflora*, *Suaeda spp.*, *P. australis*, *T. chinensis*, *S. mariqueter*, and mangroves), highlighting temporal dynamics and trends over the eight years.

Vegetation Type	2016	2017	2018	2019	2020	2021	2022	2023
S. alterniflora	23218	25918	22855	20202	22952	20201	22970	22384
Suaeda spp.	30670	27149	24436	25819	28567	32087	27484	35452
P. australis	10711	11772	10171	16349	22893	15411	15233	10614
T. chinensis	1161	2063	1159	1320	3173	2502	3449	2085
S. mariqueter	3913	4046	3019	3551	2708	2923	2203	2270
mangroves	5320	4894	5293	6203	7898	7030	6630	7648

The transition matrices (Fig. 5) derived from the classification results of 2016, 2018, 2020, and 2023 indicate that the dominant wetland vegetation types along the coast of China experienced substantial dynamics during this period. Overall, transitions among *S. alterniflora*, *Suaeda spp.*, and *P. australis* were the most frequent, whereas the distributions of *T. chinensis*, *S. mariqueter*, and mangroves remained relatively stable.

During 2016–2018, the primary transitions occurred from *Suaeda spp.* and *P. australis* to *S. alterniflora*, with transition areas of approximately 830 ha (30.5%) and 2,800 ha (26.0%), respectively. The self-persistence of *S. alterniflora* was about 7,970 ha (56.6%), higher than that of other types, indicating that most patches maintained their type between the two periods. In 2018–2020, these transitions intensified, with areas converting from *Suaeda spp.* and *P. australis* to *S. alterniflora* reaching approximately 560 ha (17.0%) and 2,910 ha (23.5%), respectively, both higher than in the previous period. The net gain of *S. alterniflora* during this interval was about 3,810 ha, representing the most pronounced expansion phase, consistent with its large-scale colonization of the lower tidal flats. During 2020–2023, the overall transition rate decreased. The reverse transitions from *S. alterniflora* to *Suaeda spp.* and *P. australis* were approximately 970 ha (8.2%) and 3,520 ha (29.6%), respectively, while conversions from *Suaeda spp.* to *S. alterniflora* still accounted for 1,720 ha (25.1%), suggesting local replacement or management interventions. The areas of change for mangroves and *T. chinensis* were both less than 200 ha (<1%), remaining concentrated in the southern estuarine regions.
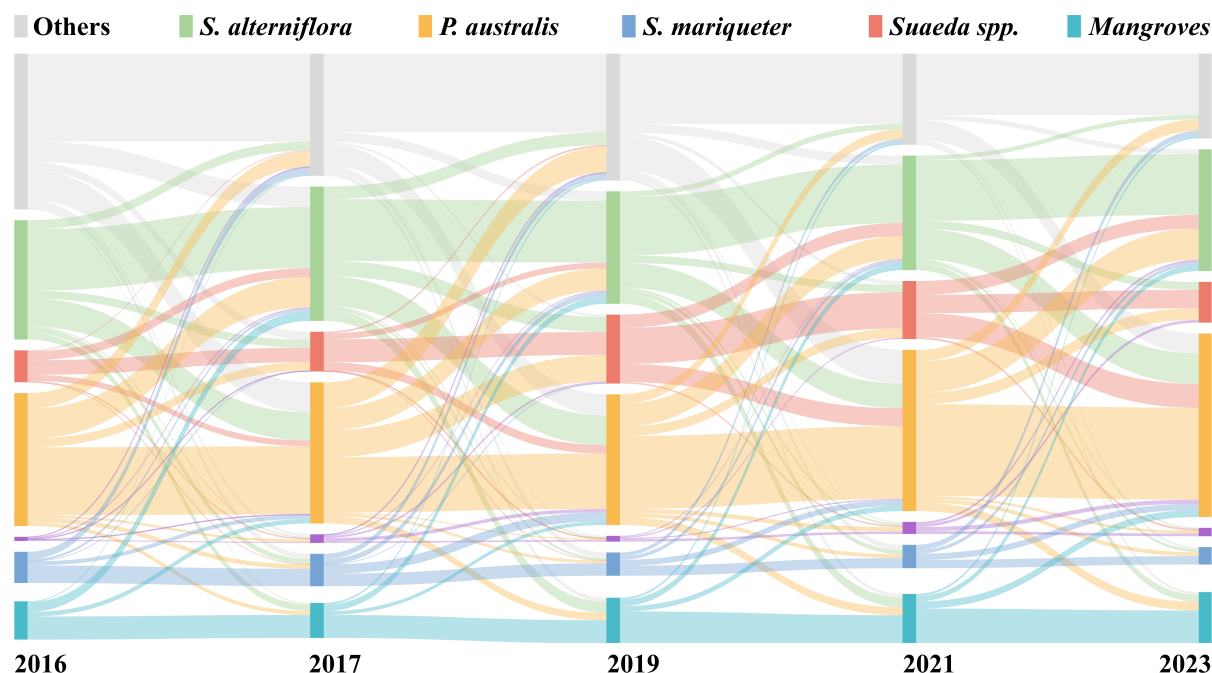
Figure 5. Sankey diagram showing the transitions among coastal wetland vegetation types in China from 2016 to 2023. The width of each flow represents the area of vegetation conversion between consecutive years, highlighting dominant succession pathways and interannual dynamics among *S. alterniflora*, *Suaeda spp.*, *P. australis*, *T. chinensis*, *S. mariqueter*, and mangroves.

4.2 Performance evaluation of P_SVCN

We collected a total of 15,558 in situ data points across the China coastal wetlands, of which 4,668 were reserved for model validation. To further evaluate the effectiveness of the proposed P_SVCN model, we compared its performance with the Salt marsh Vegetation Classification Network (SVCN) (Li et al., 2024b) on the same validation dataset. As shown in Tab. 3, P_SVCN outperformed SVCN across all vegetation classes. For *S. alterniflora*, P_SVCN achieved a producer's accuracy (PA) of 0.927, user's accuracy (UA) of 0.882, and F1 score of 0.904, compared to 0.881, 0.820, and 0.849 for SVCN. For *P. australis*, the corresponding values were 0.921, 0.880, and 0.900 for P_SVCN versus 0.876, 0.829, and 0.852 for SVCN. For *Suaeda* spp., P_SVCN yielded a PA of 0.904, UA of 0.954, and F1 score of 0.928, higher than SVCN (PA = 0.851, UA = 0.920, F1 = 0.884). Similarly, *S. mariqueter* (P_SVCN: 0.937/0.953/0.945; SVCN: 0.902/0.927/0.914), mangroves (P_SVCN: 0.918/0.979/0.948; SVCN: 0.890/0.953/0.921), and *T. chinensis* (P_SVCN: 0.846/0.813/0.829; SVCN: 0.811/0.796/0.803) also exhibited higher accuracy metrics under P_SVCN. The overall accuracy (OA) and Kappa coefficient for P_SVCN were 0.916 and 0.898, respectively, exceeding those of SVCN (OA = 0.874, Kappa = 0.845). These results indicate that the dual-branch multi-source attention design of P_SVCN effectively enhances classification performance for coastal wetland vegetation types.

Table 3. Comparison of classification accuracy between P_SVCN and SVCN for coastal wetland vegetation types. The upward arrow (↑) indicates that the P_SVCN's metric values are comparatively higher, demonstrating the P_SVCN's superior performance.

Vegetation Type	P_SVCN (this study)↑			SVCN (Li et al., 2024b)		
	PA↑	UA↑	F1↑	PA	UA	F1
S. alterniflora	0.927	0.882	0.904	0.881	0.820	0.849
P. australis	0.921	0.880	0.900	0.876	0.829	0.852
Suaeda spp.	0.904	0.954	0.928	0.851	0.920	0.884
S. mariqueter	0.937	0.953	0.945	0.902	0.927	0.914
mangroves	0.918	0.979	0.948	0.890	0.953	0.921
T. chinensis	0.846	0.813	0.829	0.811	0.796	0.803
Overall Accuracy (OA)		0.916			0.874	
Kappa		0.898			0.845	

265 The detailed confusion matrices for the P_SVCN and SVCN models are presented in Fig. 6. Rows correspond to the ground truth classes, and columns represent predicted classes. Diagonal entries indicate the number of correctly classified samples, while off-diagonal elements reflect misclassifications. P_SVCN shows consistently higher per-class accuracy compared with SVCN. The largest improvements are observed in *Suaeda spp.* and *T. chinensis*, which are often confused with neighboring species in SVCN predictions. Misclassifications in both models mainly occur between spectrally or structurally similar vegeta-

270 tion types, such as *S. alterniflora* vs. *P. australis*. This highlights the advantage of P_SVCN's multi-source feature integration, which effectively captures both SAR structural information and optical phenology for improved discriminability.
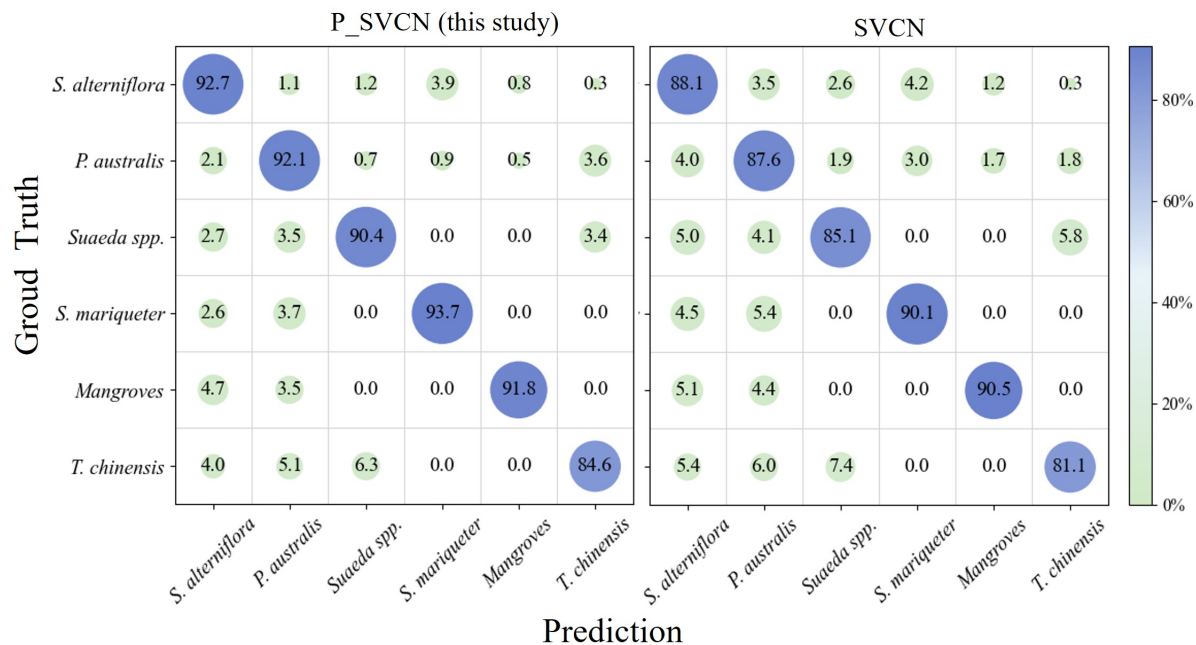
Figure 6. Comparison of confusion matrices for P_SVCN and SVCN on coastal wetland vegetation classification. The diagonal elements indicate the percentage of correctly classified samples, while the off-diagonal elements represent the percentage of misclassified samples.

5   Discussion

5.1   The CCAV-10m dataset: Filling a critical gap in coastal wetland vegetation mapping

We introduce CCAV-10m, an annual 10m coastal wetland vegetation dataset generated using the P-SVCN model, which captures the spatial and temporal dynamics of China's coastal wetland vegetation from 2016 to 2023. As the first publicly available national-scale, species-level coastal wetland dataset, CCAV-10m provides fine-resolution mapping of six representative vegetation types—*S. alterniflora*, *P. australis*, *Suaeda spp.*, *S. mariqueter*, mangroves, and *T. chinensis*. Model evaluation demonstrates robust performance, with an overall accuracy of 0.916 and a Kappa coefficient of 0.898.

Compared with existing coastal wetland datasets (Table 4), CCAV-10m demonstrates significant advantages in terms of spatial coverage, functional composition, and temporal continuity. First, regarding spatial coverage, CCAV-10m spans the entire coastal zone of China, and its 10 m resolution enables precise delineation of complex intertidal vegetation mosaics. In contrast, SaltMarshVegYRD (Zhang et al., 2021) is limited to the Yellow River Delta with a 30 m resolution, and CMSA (Li et al., 2024a), although also at 10 m resolution, focuses solely on a single invasive species, failing to systematically represent coastal vegetation patterns at the national scale. Second, in terms of functional composition, CCAV-10m provides species-level refinement, differentiating six representative vegetation types along the Chinese coast: *S. alterniflora*, *P. australis*, *Suaeda*

spp., *S. mariqueter*, mangroves, and *T. chinensis*. By comparison, CCSV(Zhao et al., 2023) classifies only broad salt marsh categories, and CMSA focuses exclusively on the invasive species *S. alterniflora*, both lacking intra-community functional differentiation. Finally, in the temporal dimension, CCAV-10m offers a continuous annual time series from 2016 to 2023, enabling long-term and systematic monitoring of coastal wetland dynamics. In contrast, CCSV contains only a single epoch in

290 2020, and CMSA provides annual sequences but only for a single species.

CCAV-10m achieves multidimensional improvements in spatial coverage, functional composition, and temporal continuity. It represents the first high-resolution coastal vegetation dataset in China with multi-species recognition and annual consistency, providing unified and high-quality baseline data for studies on coastal ecosystem succession, invasive species spread, and blue carbon assessment.

Table 4. Comparison of CCAV-10m with existing coastal wetland datasets.

Dataset	Spatial Coverage	Spatial Resolution	Functional Composition	Temporal Dimension
CCAV-10m (Ours)	China's Coastal Wetland	10 m	*S. alterniflora*, *P. australis*, *Suaeda spp.*, *S. mariqueter*, mangroves, *T. chinensis*	2016–2023
SaltMarshVegYRD (Zhang et al., 2021)	Yellow River Delta wetland	30 m	*S. alterniflora*, *P. australis*, *Suaeda spp.*	1999–2020
CCSV (Zhao et al., 2023)	China's Coastal Wetland	10 m	Salt marsh	2020
CMSA (Li et al., 2024a)	China's Coastal Wetland	10 m	*S. alterniflora*	2017–2021

295 **5.2 Provincial-scale dynamics of China's coastal wetland vegetation (2016–2023)**

Coastal wetland vegetation exhibited clear provincial-scale differences in China from 2016 to 2023. In Liaoning Province, the dominant vegetation types included *S. alterniflora*, *Suaeda* spp., and *P. australis*. Hebei, Shandong, and Tianjin showed similar compositions, characterized mainly by *S. alterniflora*, *Suaeda* spp., and *P. australis*, with additional occurrences of *T. chinensis* in specific areas. In Jiangsu Province, coastal wetlands were primarily dominated by *S. alterniflora*, *Suaeda* spp., and

300 *P. australis*. Shanghai featured a vegetation assemblage composed of *S. alterniflora*, *S. mariqueter*, and *P. australis*. In Zhejiang Province, *S. alterniflora* and *S. mariqueter* were widely distributed, accompanied by patches of mangroves and *P. australis*. Fujian Province, located at the southernmost part of the study area, was characterized by extensive mangrove ecosystems, with additional distributions of *S. alterniflora* and *P. australis*.

Coastal wetlands showed clear provincial differences in area and species composition. Jiangsu, Shandong, and Zhejiang had
305   the largest wetland areas, followed by Fujian, Liaoning, and Shanghai, while Hebei and Tianjin were smaller. *S. alterniflora* and
P. australis dominated most provinces, with *Suaeda spp.*, *T. chinensis*, *S. mariqueter*, and mangroves restricted but ecologically
important. In Liaoning, wetlands were stable, dominated by *P. australis* (450–530 ha) and *S. alterniflora* (450–9,030 ha). Tian-
jin had scattered wetlands (400–780 ha) with alternating dominance of *P. australis* and *Suaeda spp.*. Hebei showed pronounced
species dynamics, with *S. alterniflora* stable (1,320–2,420 ha) and *P. australis* increasing from 2,870 to 3,730 ha. Shandong
310   experienced significant changes, *P. australis* rising from 3,910 to 7,120 ha, reflecting Spartina control effects. Jiangsu, the
largest coastal wetland province, had over 60% combined *S. alterniflora* and *P. australis*, with *P. australis* slightly increasing
from 3,740 to 4,710 ha. In Shanghai, wetlands shrank from 1,300 to 970 ha, while *S. mariqueter* partially recovered post-2021.
Zhejiang's wetlands alternated between *S. alterniflora* and *P. australis* (2,990–5,240 ha), and *S. mariqueter* remained stable
(2,110–4,210 ha). Fujian's wetlands were relatively stable (2,290–3,850 ha), dominated by *S. alterniflora*. Coastal wetlands
315   exhibited clear provincial differences, with *S. alterniflora* and *P. australis* dominating most regions, while *Suaeda spp.*, *T.
chinensis*, *S. mariqueter*, and mangroves were more restricted in distribution yet remained ecologically significant, reflecting
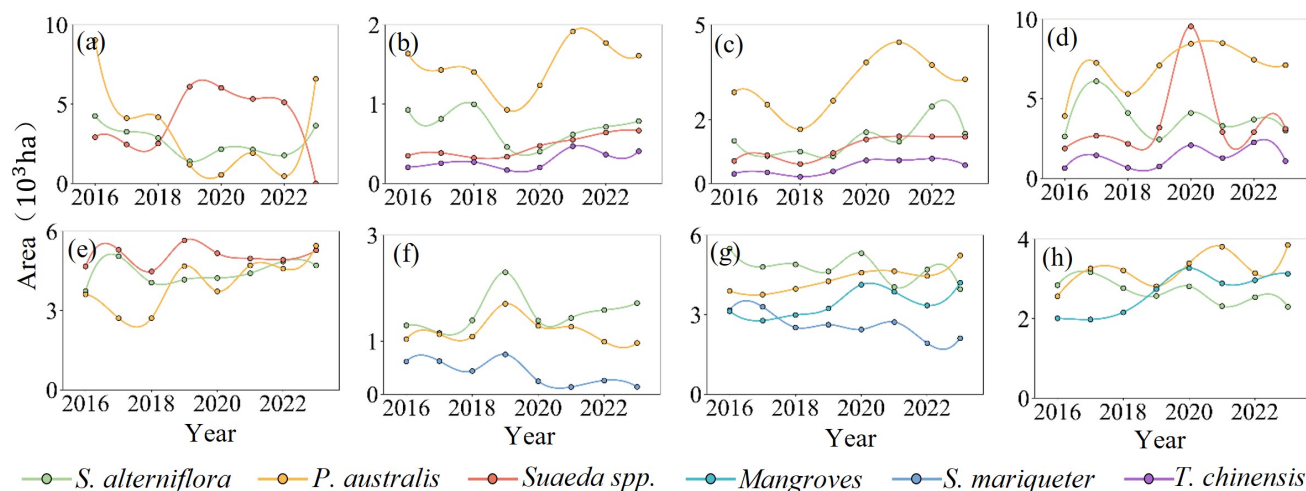localized dynamic adjustments within a generally stable vegetation structure.

Figure 7. Temporal dynamics of wetland vegetation area in eight Chinese coastal provinces from 2016 to 2023. (a) Liaoning, (b)
Tianjin, (c) Hebei, (d) Shandong, (e) Jiangsu, (f) Shanghai, (g) Zhejiang, and (h) Fujian.

5.3   Uncertainty analysis of the CCAV-10m dataset

Despite the high overall classification accuracy of the CCAV-10m dataset (OA = 0.916), certain uncertainties remain (Tab. 5).
320   To quantitatively evaluate potential sources of error, we conducted ablation experiments comparing three input configurations:
Sentinel-1 only (S1), Sentinel-2 only (S2, dual-temporal composite), and the S1+S2 fusion mode. The overall accuracies were

0.895, 0.870, and 0.916, respectively, indicating significant complementarity between radar and optical information in intertidal wetland vegetation identification.

325 From the classification results, the S1-only configuration slightly outperformed S2 in most vegetation types, particularly in the discrimination of *S. alterniflora* and *P. australis*. Sentinel-1 C-band SAR captures canopy structure, surface roughness, and moisture scattering features (Zhang et al., 2022a; Mleczko and Mróz, 2018; Rajngewerc et al., 2022), which are less sensitive to optical disturbances caused by turbid water and cloudy conditions, thus providing advantages in identifying structurally distinct vegetation. In contrast, the S2-only configuration, although leveraging dual-temporal imagery to enhance spectral temporal information, is affected by surface albedo variations and spectral mixing in intertidal zones (Feng et al., 2022), resulting

330 in misclassifications between spectrally similar types such as *Suaeda spp.* and *T. chinensis*. The S1+S2 fusion significantly improved per-class producer's accuracy (PA) and user's accuracy (UA), effectively mitigating the limitations of single data sources. The structural and moisture information from SAR complements the spectral and vegetation index features from optical imagery, enabling stable model performance across different tidal stages and climatic conditions, particularly enhancing the separability of *Suaeda spp.* and *T. chinensis*.

335 Nevertheless, residual uncertainties persist. First, *T. chinensis* and *Suaeda spp.* are often interspersed in the upper wetland, with similar temporal and phenological characteristics (Gao et al., 2015; Jiao et al., 2021; Wu et al., 2020), making complete discrimination challenging even under multi-source fusion. Second, *Scirpus mariqueter* has a narrow and highly patchy distribution (Gu et al., 2021), which may result in omission errors under 10 m resolution. Future studies could integrate higher-resolution SAR data (e.g., TerraSAR-X, GF-3) and phenology-based temporal compositing strategies to further reduce

340 classification uncertainty and enhance spatiotemporal consistency.

Table 5. Comparison of producer's accuracy (PA) and user's accuracy (UA) for different input configurations: Sentinel-1 (S1), Sentinel-2 (S2, dual-temporal), and S1+S2 fusion. The upward arrow (↑) indicates that the S1+S2 configuration achieves comparatively higher metric values, demonstrating its superior performance.

Class	PA (S1)	PA (S2)	PA (S1+S2)↑	UA (S1)	UA (S2)	UA (S1+S2)↑
S. alterniflora	0.913	0.887	0.927	0.859	0.879	0.882
P. australis	0.898	0.868	0.921	0.853	0.857	0.880
Suaeda spp.	0.883	0.852	0.904	0.939	0.842	0.954
S. mariqueter	0.924	0.901	0.937	0.943	0.891	0.953
Mangroves	0.891	0.851	0.918	0.975	0.837	0.979
T. chinensis	0.800	0.762	0.846	0.747	0.782	0.813
Overall Accuracy (OA)	0.895	0.870	0.916	-	-	-

6 Conclusions

This study developed a phenology-guided coastal wetland vegetation classification network integrating Sentinel-1/ (P_SVCN) and generated the CCAV-10m dataset, which maps the coastal wetland vegetation types in China from 2016 to 2023. By integrating multi-source Sentinel-1 SAR and Sentinel-2 MSI data, the P_SVCN fully exploits structural and phenological features,
345   enabling accurate discrimination of spectrally similar and spatially fragmented vegetation types. The results are summarized as follows:

(1) A long-term, high-resolution species-level vegetation dataset (CCAV-10m).The dataset provides annual species-level maps of coastal wetland vegetation at a spatial resolution of 10 m, distinguishing six dominant plant types. Spatiotemporal analysis shows that *Suaeda spp.* is the predominant vegetation type, followed by *S. alterniflora*, whose coverage nearly
350   matches the combined extent of *P. australis*, mangroves, *S. mariqueter*, and *T. chinensis*. Further temporal assessments reveal pronounced community succession in recent years, including the continued expansion of *S. alterniflora* and *Suaeda spp.*, fluctuating patterns in *P. australis*, and a steady increase in mangrove extent. Transition matrices indicate that conversions among *S. alterniflora*, *Suaeda spp.*, and *P. australis* occurs most frequently, reflecting the dynamic responses of coastal wetland ecosystems to natural processes and human activities.

355   (2) A novel phenology-guided deep-learning framework (P_SVCN). The P_SVCN model exhibits strong classification performance, achieving an overall accuracy of 0.916 and a Kappa coefficient of 0.898 based on validation with 4,668 in situ samples. These results exceed those of the baseline SVCN model (overall accuracy 0.874, Kappa 0.845). Ablation experiments further demonstrate the complementary strengths of Sentinel-1 synthetic aperture radar and Sentinel-2 optical observations, particularly in distinguishing vegetation types with highly similar spectral properties or fragmented spatial patterns.

360   CCAV-10m effectively bridges the gap between coarse-resolution ecosystem maps and single-species products by balancing species-level classification accuracy and large-scale spatial coverage. The dataset provides high-precision spatiotemporal information for monitoring vegetation succession, assessing invasive species, estimating blue carbon stocks, and supporting ecological restoration planning. Moreover, it offers a robust foundation for sustainable coastal ecosystem management under global environmental change. The CCAV-10m dataset is publicly available at https://doi.org/10.57760/sciencedb.31077,
365   supporting reproducibility and further applications in related research.

Author contributions. LYY designed the research. LYY and LT performed the experiments and code. LYY wrote the manuscript. LT, SZJ, YS and ZZL process data analysis. LM and YLN provided the resource. LM and YLN supervised and reviewed the manuscript.

375 *Competing interests.* The contact author has declared that none of the authors has any competing interests.

Disclaimer. To access the datasets associated with this study, users should comply with the corresponding data access policies and usage requirements. The CCAV-10m dataset is distributed under the Creative Commons Attribution 4.0 International License (CC BY 4.0).

References

Aburto-Oropeza, O., Ezcurra, E., Danemann, G., Valdez, V., Murray, J., and Sala, E.: Mangroves in the Gulf of California increase fishery yields, Proceedings of the National Academy of Sciences, 105, 10 456–10 459, https://doi.org/10.1073/pnas.0804601105, 2008.

Almond, D., Chen, Y., Greenstone, M., and Li, H.: Winter heating or clean air? Unintended impacts of China's Huai river policy, American Economic Review, 99, 184–190, https://doi.org/10.1257/aer.99.2.184, 2009.

Bao, Y., Lin, X., Jia, M., Xiao, Z., Wang, C., Liao, J., and Zhang, Y.: Convergence in key month of phenology-based mangrove species classification using sentinel-2 imagery data: insights from structural and physiological indices, International Journal of Digital Earth, 18, 2528 651, https://doi.org/10.1080/17538947.2025.2528651, 2025.

Bernhardt, E.: Coastal freshwater wetlands squeezed between migrating salt marshes and working lands, Science Advances, 8, eadd1628, https://doi.org/10.1126/sciadv.add1628, 2022.

Bertram, C., Quaas, M., Reusch, T. B., Vafeidis, A. T., Wolff, C., and Rickels, W.: The blue carbon wealth of nations, Nature Climate Change, 11, 704–709, https://doi.org/10.1038/s41558-021-01089-4, 2021.

Cao, W. and Wong, M. H.: Current status of coastal zone issues and management in China: a review, Environment International, 33, 985–992, https://doi.org/10.1016/j.envint.2007.04.009, 2007.

Chen, C., Chen, Y., Liu, Z., Xue, Z., Yang, G., and Sun, W.: PCSAI: a phenological characteristics-based Spartina alterniflora index derived from a time-series of remote sensing images, Big Earth Data, pp. 1–29, https://doi.org/10.1080/20964471.2025.2554043, 2025.

Chen, G., Jin, R., Ye, Z., Li, Q., Gu, J., Luo, M., Luo, Y., Christakos, G., Morris, J., He, J., et al.: Spatiotemporal mapping of salt marshes in the intertidal zone of China during 1985–2019, Journal of Remote Sensing, https://doi.org/10.34133/2022/9793626, 2022.

Chen, Y., Ebenstein, A., Greenstone, M., and Li, H.: Evidence on the impact of sustained exposure to air pollution on life expectancy from China's Huai River policy, Proceedings of the National Academy of Sciences, 110, 12 936–12 941, https://doi.org/10.1073/pnas.1300018110, 2013.

Costanza, R., De Groot, R., Sutton, P., Van der Ploeg, S., Anderson, S. J., Kubiszewski, I., Farber, S., and Turner, R. K.: Changes in the global value of ecosystem services, Global environmental change, 26, 152–158, https://doi.org/10.1016/j.gloenvcha.2014.04.002, 2014.

Day, J., Anthony, E., Costanza, R., Edmonds, D., Gunn, J., Hopkinson, C., Mann, M. E., Morris, J., Osland, M., Quirk, T., et al.: Coastal wetlands in the Anthropocene, Annual Review of Environment and Resources, 49, 105–135, https://doi.org/10.1146/annurev-environ-121922-041109, 2024.

Duarte, C. M., Losada, I. J., Hendriks, I. E., Mazarrasa, I., and Marbà, N.: The role of coastal plant communities for climate change mitigation and adaptation, Nature climate change, 3, 961–968, https://doi.org/10.1038/nclimate1970, 2013.

Feng, K., Mao, D., Qiu, Z., Zhao, Y., and Wang, Z.: Can time-series Sentinel images be used to properly identify wetland plant communities?, GIScience & Remote Sensing, 59, 2202–2216, https://doi.org/10.1080/15481603.2022.2156064, 2022.

Ferro, A., Brunner, D., Bruzzone, L., and Lemoine, G.: On the relationship between double bounce and the orientation of buildings in VHR SAR images, IEEE Geoscience and Remote Sensing Letters, 8, 612–616, https://doi.org/10.1109/LGRS.2010.2097580, 2011.

Fu, B., Yuan, B., Yao, H., Sun, W., Jia, M., Yao, Z., and Wang, Y.: Spatio-temporal dynamics of invasive Spartina alterniflora and its functional traits' responding to hydro-meteorology, Earth's Future, 13, e2024EF005 421, https://doi.org/10.1029/2024EF005421, 2025.

Gabler, C. A., Osland, M. J., Grace, J. B., Stagg, C. L., Day, R. H., Hartley, S. B., Enwright, N. M., From, A. S., McCoy, M. L., and McLeod, J. L.: Macroclimatic change expected to transform coastal wetland ecosystems this century, Nature Climate Change, 7, 142–147, https://doi.org/10.1038/nclimate3203, 2017.

Gallo, K., Ji, L., Reed, B., Eidenshink, J., and Dwyer, J.: Multi-platform comparisons of MODIS and AVHRR normalized difference vegetation index data, Remote Sensing of Environment, 99, 221–231, https://doi.org/10.1016/j.rse.2005.08.014, 2005.

420   Gao, M., Wang, X., Hui, C., Yi, H., Zhang, C., Wu, X., Bi, X., Wang, Y., Xiao, L., and Wang, D.: Assembly of plant communities in coastal wetlands—the role of saltcedar Tamarix chinensis during early succession, Journal of Plant Ecology, 8, 539–548, https://doi.org/10.1093/jpe/rtu037, 2015.

Gao, Y., Hu, Z., Wang, Z., Shi, Q., Chen, D., Wu, S., Gao, Y., and Zhang, Y.: Phenology metrics for vegetation type classification in estuarine wetlands using satellite imagery, Sustainability, 15, 1373, https://doi.org/10.3390/su15021373, 2023.

425   Gu, J., Jin, R., Chen, G., Ye, Z., Li, Q., Wang, H., Li, D., Christakos, G., Agusti, S., Duarte, C. M., et al.: Areal extent, species composition, and spatial distribution of coastal saltmarshes in China, IEEE Journal of Selected Topics in Applied Earth Observations and Remote Sensing, 14, 7085–7094, https://doi.org/10.1109/JSTARS.2021.3093673, 2021.

Gu, J., Wu, J., and Xie, D.: Coastal salt marsh changes in China: Landscape pattern, driving factors, and carbon dynamics, Geography and Sustainability, p. 100281, https://doi.org/10.1016/j.geosus.2025.100281, 2025.

430   Hu, Y., Tian, B., Yuan, L., Li, X., Huang, Y., Shi, R., Jiang, X., Sun, C., et al.: Mapping coastal salt marshes in China using time series of Sentinel-1 SAR, ISPRS Journal of Photogrammetry and Remote Sensing, 173, 122–134, https://doi.org/10.1016/j.isprsjprs.2021.01.003, 2021.

Jiao, L., Zhang, Y., Sun, T., Yang, W., Shao, D., Zhang, P., and Liu, Q.: Spatial analysis as a tool for plant population conservation: A case study of Tamarix chinensis in the Yellow River Delta, China, Sustainability, 13, 8291, https://doi.org/10.3390/su13158291, 2021.

435   Kang, B., Chen, X., Du, Z., Meng, W., and Li, H.: Species-based mapping of carbon stocks in salt marsh: Tianjin coastal zone as a case study, Ecosystem Health and Sustainability, 9, 0052, https://doi.org/10.34133/ehs.0052, 2023.

Kumar, L. and Sinha, P.: Mapping salt-marsh land-cover vegetation using high-spatial and hyperspectral satellite data to assist wetland inventory, GIScience & Remote Sensing, 51, 483–497, https://doi.org/10.1080/15481603.2014.947838, 2014.

Li, H., Wang, C., Cui, Y., and Hodgson, M.: Mapping salt marsh along coastal South Carolina using U-Net, ISPRS Journal of Photogrammetry
440   and Remote Sensing, 179, 121–132, https://doi.org/10.1016/j.isprsjprs.2021.07.011, 2021a.

Li, H., Zhang, C., Zhang, S., Ding, X., and Atkinson, P. M.: Iterative Deep Learning (IDL) for agricultural landscape classification using fine spatial resolution remotely sensed imagery, International Journal of Applied Earth Observation and Geoinformation, 102, 102 437, https://doi.org/10.1016/j.jag.2021.102437, 2021b.

Li, X., Tian, J., Li, X., Yu, Y., Ou, Y., Zhu, L., Zhu, X., Zhou, B., and Gong, H.: Annual mapping of Spartina alterniflora with deep learning
445   and spectral-phenological features from 2017 to 2021 in the mainland of China, International Journal of Remote Sensing, 45, 3172–3199, https://doi.org/10.1080/01431161.2024.2343136, 2024a.

Li, Y., Yuan, L., Song, Z., Yu, S., Zhang, X., Tian, B., and Liu, M.: Salt marsh carbon stock estimation using deep learning with Sentinel-1 SAR of the Yangtze River estuary, China, International Journal of Applied Earth Observation and Geoinformation, 133, 104 138, https://doi.org/10.1016/j.jag.2024.104138, 2024b.

450   Li, Y., TingLiu, Yuan, L., Song, Z., Yang, S., Zhu, Z., and Liu, M.: CCAV-10m: An Annual Spatiotemporal China Coastal Wetland Vegetation Dataset Integrating Sentinel-1/2 Observations via Deep Learning, https://doi.org/10.57760/sciencedb.31077, 2025.

Luo, J., Wu, X., Gao, Y., Cai, Y., Yang, L., Xiong, Y., Yang, Q., Liu, J., Li, Y., Deng, Z., et al.: Spatiotemporal Variations and Seasonal Climatic Driving Factors of Stable Vegetation Phenology Across China over the Past Two Decades, Remote Sensing, 17, 3467, https://doi.org/10.3390/rs17203467, 2025.

455   Luther, D. A. and Greenberg, R.: Mangroves: a global perspective on the evolution and conservation of their terrestrial vertebrates, Bio-Science, 59, 602–612, https://doi.org/10.1525/bio.2009.59.7.11, 2009.

Macreadie, P. I., Anton, A., Raven, J. A., Beaumont, N., Connolly, R. M., Friess, D. A., Kelleway, J. J., Kennedy, H., Kuwae, T., Lavery, P. S., et al.: The future of Blue Carbon science, Nature communications, 10, 3998, https://doi.org/10.1038/s41467-019-11693-w, 2019.

Mahdianpari, M., Jafarzadeh, H., Granger, J. E., Mohammadimanesh, F., Brisco, B., Salehi, B., Homayouni, S., and Weng, Q.: A large-scale

460   change monitoring of wetlands using time series Landsat imagery on Google Earth Engine: a case study in Newfoundland, GIScience & Remote Sensing, 57, 1102–1124, https://doi.org/10.1080/15481603.2020.1846948, 2020.

Mandal, D., Kumar, V., Ratha, D., Dey, S., Bhattacharya, A., Lopez-Sanchez, J. M., McNairn, H., and Rao, Y. S.: Dual polarimetric radar vegetation index for crop growth monitoring using sentinel-1 SAR data, Remote Sensing of Environment, 247, 111 954, https://doi.org/10.1016/j.rse.2020.111954, 2020.

465   Mao, W., Wang, X., Liu, G., Pirasteh, S., Zhang, R., Lin, H., Xie, Y., Xiang, W., Ma, Z., and Ma, P.: Time series InSAR ionospheric delay estimation, correction, and ground deformation monitoring with reformulating range split-spectrum interferometry, IEEE Transactions on Geoscience and Remote Sensing, 61, 1–18, https://doi.org/10.1109/TGRS.2023.3298919, 2023.

Min, Y., Ke, Y., Zhuo, Z., Qi, W., Li, J., Li, P., and Zhao, N.: Monitoring Spartina Alterniflora removal dynamics across coastal China using time series Sentinel-1 imagery, Remote Sensing of Environment, 326, 114 813, https://doi.org/10.1016/j.rse.2025.114813, 2025.

470   Mleczko, M. and Mróz, M.: Wetland mapping using sar data from the sentinel-1a and tandem-x missions: A comparative study in the biebrza floodplain (Poland), Remote Sensing, 10, 78, https://doi.org/10.3390/rs10010078, 2018.

Morales-Barquero, L., Lyons, M. B., Phinn, S. R., and Roelfsema, C. M.: Trends in remote sensing accuracy assessment approaches in the context of natural resources, Remote sensing, 11, 2305, https://doi.org/10.3390/rs11192305, 2019.

Moreno-Mateos, D., Power, M. E., Comín, F. A., and Yockteng, R.: Structural and functional loss in restored wetland ecosystems, PLoS

475   biology, 10, e1001 247, https://doi.org/10.1371/journal.pbio.1001247, 2012.

Nikaein, T., Iannini, L., Molijn, R. A., and Lopez-Dekker, P.: On the value of Sentinel-1 InSAR coherence time-series for vegetation classification, Remote Sensing, 13, 3300, https://doi.org/10.3390/rs13163300, 2021.

O'Connell, J. L., Mishra, D. R., Cotten, D. L., Wang, L., and Alber, M.: The Tidal Marsh Inundation Index (TMII): An inundation filter to flag flooded pixels and improve MODIS tidal marsh vegetation time-series analysis, Remote Sensing of Environment, 201, 34–46,

480   https://doi.org/10.1016/j.rse.2017.08.008, 2017.

Potin, P., Rosich, B., Grimont, P., Miranda, N., Shurmer, I., O'Connell, A., Torres, R., and Krassenburg, M.: Sentinel-1 mission status, in: International Geoscience and Remote Sensing Symposium (IGARSS) (Vol. 2015–Novem), vol. 2015–Novem, pp. 2820–2823, IEEE, https://doi.org/10.1109/IGARSS.2015.7326401, 2015.

Rajngewerc, M., Grimson, R., Bali, L., Minotti, P., and Kandus, P.: Cover classifications in wetlands using Sentinel-1 data (Band C): a case

485   study in the Parana river delta, Argentina, Revista de Teledetección, pp. 29–46, https://doi.org/10.4995/raet.2022.16915, 2022.

Schuerch, M., Spencer, T., Temmerman, S., Kirwan, M. L., Wolff, C., Lincke, D., McOwen, C. J., Pickering, M. D., Reef, R., Vafeidis, A. T., et al.: Future response of global coastal wetlands to sea-level rise, Nature, 561, 231–234, https://doi.org/10.1038/s41586-018-0476-5, 2018.

Simioni, J. P. D., Guasselli, L. A., Nascimento, V. F., Ruiz, L. F. C., and Belloli, T. F.: Integration of multi-sensor analysis and decision

490   tree for evaluation of dual and quad-Pol SAR in L-and C-bands applied for marsh delineation, Environ. Dev. Sustain, 22, 5603–5620, https://doi.org/10.1007/s10668-019-00442-0, 2020.

Slagter, B., Tsendbazar, N.-E., Vollrath, A., and Reiche, J.: Mapping wetland characteristics using temporally dense Sentinel-1 and Sentinel-2 data: A case study in the St. Lucia wetlands, South Africa, International Journal of Applied Earth Observation and Geoinformation, 86, 102 009, https://doi.org/10.1016/j.jag.2019.102009, 2020.

495 Song, Z. and Zhong, B.: A lightweight local-global attention network for single image super-resolution, in: Proceedings of the Asian conference on computer vision, pp. 4395–4410, https://doi.org/10.1007/978-3-031-26351-4_37, 2022.

Sun, B., Zhang, D., and Lai, Z.: Coastal salt marsh vegetation classification using hybrid convolutional neural networks and spectral index time series images, Ecological Indicators, 178, 113 996, https://doi.org/10.1016/j.ecolind.2025.113996, 2025.

Sun, C., Li, J., Liu, Y., Liu, Y., and Liu, R.: Plant species classification in salt marshes using phenological parameters derived from Sentinel-2
500 pixel-differential time-series, Remote Sensing of Environment, 256, 112 320, https://doi.org/10.1016/j.rse.2021.112320, 2021.

Sun, C., Li, J., Liu, Y., Zhao, S., Zheng, J., and Zhang, S.: Tracking annual changes in the distribution and composition of saltmarsh vegetation on the Jiangsu coast of China using Landsat time series–based phenological parameters, Remote Sensing of Environment, 284, 113 370, https://doi.org/10.1016/j.rse.2022.113370, 2023.

Sun, L.: Survey Dataset of Wetland Plants in Coastal Areas of China (2013-2017), https://doi.org/10.57760/sciencedb.IGA.00342, 2023.

505 Sun, Z., Sun, W., Tong, C., Zeng, C., Yu, X., and Mou, X.: China's coastal wetlands: conservation history, implementation efforts, existing issues and strategies for future improvement, Environment International, 79, 25–41, https://doi.org/10.1016/j.envint.2015.02.017, 2015.

Takeuchi, W., Tamura, M., and Yasuoka, Y.: Estimation of methane emission from West Siberian wetland by scaling technique between NOAA AVHRR and SPOT HRV, Remote Sensing of Environment, 85, 21–29, https://doi.org/10.1016/S0034-4257(02)00183-9, 2003.

Tian, J., Wang, L., Yin, D., Li, X., Diao, C., Gong, H., Shi, C., Menenti, M., Ge, Y., Nie, S., et al.: Development of spectral-
510 phenological features for deep learning to understand Spartina alterniflora invasion, Remote Sensing of Environment, 242, 111 745, https://doi.org/10.1016/j.rse.2020.111745, 2020.

Van Beijma, S., Comber, A., and Lamb, A.: Random forest classification of salt marsh vegetation habitats using quad-polarimetric airborne SAR, elevation and optical RS data, Remote Sensing of Environment, 149, 118–129, https://doi.org/10.1016/j.rse.2014.04.010, 2014.

Veloso, A., Mermoz, S., Bouvet, A., Le Toan, T., Planells, M., Dejoux, J.-F., and Ceschia, E.: Understanding the temporal be-
515 havior of crops using Sentinel-1 and Sentinel-2-like data for agricultural applications, Remote Sens. Environ., 199, 415–426, https://doi.org/10.1016/j.rse.2017.07.015, 2017.

Vreugdenhil, M., Wagner, W., Bauer-Marschallinger, B., Pfeil, I., Teubner, I., Rüdiger, C., and Strauss, P.: Sensitivity of Sentinel-1 backscatter to vegetation dynamics: An Austrian case study, Remote Sensing, 10, 1396, https://doi.org/10.3390/rs10091396, 2018.

Wang, X., Xiao, X., Xu, X., Zou, Z., Chen, B., Qin, Y., Zhang, X., Dong, J., Liu, D., Pan, L., et al.: Rebound in China's coastal wetlands
520 following conservation and restoration, Nature Sustainability, 4, 1076–1083, https://doi.org/10.1038/s41893-021-00793-5, 2021.

Wang, Y., Jin, S., and Dardanelli, G.: Vegetation classification and evaluation of yancheng coastal wetlands based on random forest algorithm from sentinel-2 images, Remote Sensing, 16, 1124, https://doi.org/10.3390/rs16071124, 2024.

Webb, E. L., Friess, D. A., Krauss, K. W., Cahoon, D. R., Guntenspergen, G. R., and Phelps, J.: A global standard for monitoring coastal wetland vulnerability to accelerated sea-level rise, Nature Climate Change, 3, 458–465, https://doi.org/10.1038/nclimate1756, 2013.

525 Wei, S., Zhang, H., Xu, Z., Lin, G., Lin, Y., Liang, X., Ling, J., Wee, A. K. S., Lin, H., Zhou, Y., et al.: Coastal urbanization may indirectly positively impact growth of mangrove forests, Communications Earth & Environment, 5, 608, https://doi.org/10.1038/s43247-024-01776-y, 2024.

Wu, Y., Dai, L., Wang, Y., Xie, L., Zhao, S., Liu, Y., Zhang, M., and Zhang, Z.: Coexistence mechanisms of Tamarix chinensis and Suaeda salsa in the Yellow River Delta, China, Environmental Science and Pollution Research, 27, 26 172–26 181, https://doi.org/10.1007/s11356-020-08883-1, 2020.

Xu, R., Fan, Y., Fan, B., Feng, G., and Li, R.: Classification and Monitoring of Salt Marsh Vegetation in the Yellow River Delta Based on Multi-Source Remote Sensing Data Fusion, Sensors, 25, 529, https://doi.org/10.3390/s25020529, 2025.

Yang, R.-M. and Guo, W.-W.: Using Sentinel-1 imagery for soil salinity prediction under the condition of coastal restoration, IEEE Journal of Selected Topics in Applied Earth Observations and Remote Sensing, 12, 1482–1488, https://doi.org/10.1109/JSTARS.2019.2906064, 2019.

You, S., Loh, P., Li, Z., Qin, H., Pradit, S., Le, T. P. Q., Oeurng, C., Mohamed, C. A. R., Lee, C. W., Lu, X., et al.: Geochemical behavior of sedimentary phosphorus species in northernmost artificial mangroves in China, Forests, 13, 610, https://doi.org/10.3390/f13040610, 2022.

Zeng, J., Sun, Y., Cao, P., and Wang, H.: A phenology-based vegetation index classification (PVC) algorithm for coastal salt marshes using Landsat 8 images, International Journal of Applied Earth Observation and Geoinformation, 110, 102 776, https://doi.org/10.1016/j.jag.2022.102776, 2022.

Zhang, A., Sun, G., Ma, P., Jia, X., Ren, J., Huang, H., and Zhang, X.: Coastal wetland mapping with Sentinel-2 MSI imagery based on gravitational optimized multilayer perceptron and morphological attribute profiles, Remote Sensing, 11, 952, https://doi.org/10.3390/rs11080952, 2019.

Zhang, B., Wdowinski, S., Gann, D., Hong, S.-H., and Sah, J.: Spatiotemporal variations of wetland backscatter: The role of water depth and vegetation characteristics in Sentinel-1 dual-polarization SAR observations, Remote Sensing of Environment, 270, 112 864, https://doi.org/10.1016/j.rse.2021.112864, 2022a.

Zhang, C., Gong, Z., Qiu, H., Zhang, Y., and Zhou, D.: Mapping typical salt-marsh species in the Yellow River Delta wetland supported by temporal-spatial-spectral multidimensional features, Science of the total environment, 783, 147 061, https://doi.org/10.1016/j.scitotenv.2021.147061, 2021.

Zhang, J., Chen, S., Wu, Z., and Fu, Y. H.: Review of vegetation phenology trends in China in a changing climate, Progress in Physical Geography: Earth and Environment, 46, 829–845, https://doi.org/10.1177/03091333221114737, 2022b.

Zhang, J., Zhang, Y., Cong, N., Tian, L., Zhao, G., Zheng, Z., Gao, J., Zhu, Y., and Zhang, Y.: Coarse spatial resolution remote sensing data with AVHRR and MODIS miss the greening area compared with the Landsat data in Chinese drylands, Frontiers in Plant Science, 14, 1129 665, https://doi.org/10.3389/fpls.2023.1129665, 2023a.

Zhang, X., Liu, L., Zhao, T., Chen, X., Lin, S., Wang, J., Mi, J., and Liu, W.: GWL_FCS30: global 30 m wetland map with fine classification system using multi-sourced and time-series remote sensing imagery in 2020, Earth System Science Data Discussions, 2022, 1–31, https://doi.org/10.5194/essd-15-265-2023, 2022c.

Zhang, X., Zhao, T., Xu, H., Liu, W., Wang, J., Chen, X., and Liu, L.: GLC_FCS30D: The first global 30-m land-cover dynamic monitoring product with a fine classification system from 1985 to 2022 using dense time-series Landsat imagery and continuous change-detection method, Earth System Science Data Discussions, 2023, 1–32, https://doi.org/10.5194/essd-16-1353-2024, 2023b.

Zhao, C., Jia, M., Wang, Z., Mao, D., and Wang, Y.: Toward a better understanding of coastal salt marsh mapping: A case from China using dual-temporal images, Remote Sensing of Environment, 295, 113 664, https://doi.org/10.1016/j.rse.2023.113664, 2023.

Zhao, X., Nishina, K., Izumisawa, H., Masutomi, Y., Osako, S., and Yamamoto, S.: Monsoon Asia Rice Calendar (MARC): a gridded rice calendar in monsoon Asia based on Sentinel-1 and Sentinel-2 images, Earth System Science Data, 16, 3893–3911, https://doi.org/10.5194/essd-16-3893-2024, 2024.

Zheng, J., Sun, C., Zhao, S., Hu, M., Zhang, S., and Li, J.: Classification of salt marsh vegetation in the Yangtze River Delta of China using the pixel-level time-series and XGBoost algorithm, Journal of Remote Sensing, 3, 0036, https://doi.org/10.1080/20964471.2025.2554043, 2023.